Rapid and accurate polarimetric radar measurements of ice crystal fabric orientation at the Western Antarctic Ice Sheet (WAIS) Divide deep ice core site

Tun Jan Young[1], Carlos Martín[2], Poul Christoffersen[1], Dustin M. Schroeder[3,4], Slawek M. Tulaczyk[5], and Eliza J. Dawson[3]

[1]Scott Polar Research Institute, University of Cambridge, Cambridge CB2 1ER, United Kingdom
[2]British Antarctic Survey, Natural Environment Research Council, Cambridge CB3 0ET, United Kingdom
[3]Department of Geophysics, Stanford University, Stanford, CA 94305, USA
[4]Department of Electrical Engineering, Stanford University, Stanford, CA 94305, USA
[5]Department of Earth and Planetary Sciences, University of California, Santa Cruz, CA 95064, USA

Correspondence: T. J. Young (tjy22@cam.ac.uk)

Abstract. The Crystal Orientation Fabric (COF) of ice sheets records the past history of ice sheet deformation and influences present-day ice flow dynamics. Though not widely implemented, coherent ice-penetrating radar is able to detect anisotropic COF patterns by exploiting the birefringence of ice crystals at radar frequencies. Most previous radar studies quantify COF at a coarse azimuthal resolution limited by the number of observations made with a pair of antennas along an acquisition plane that
5 rotates around an azimuth centre. In this study, we instead conduct a suite of quad-polarimetric measurements consisting of four orthogonal antenna orientation combinations at the Western Antarctic Ice Sheet (WAIS) Divide Deep Ice Core site. From these measurements, we are able to quantify COF at this site to a depth of 1500 m at azimuthal and depth resolutions of up to $1°$ and 15 m. Our estimates of fabric asymmetry closely match corresponding fabric estimates directly measured from the WAIS Divide Deep Ice Core. While ice core studies are often unable to determine the absolute fabric orientation due to core rotation
10 during extraction, we are able to unambiguously identify and conclude that the fabric orientation is depth-invariant to at least 1500 m, equivalent to 7400 years BP (years before 1950), and coincides exactly with the modern surface strain direction at WAIS Divide. Our results support the claim that the deformation regime at WAIS Divide has not changed substantially through the majority of the Holocene. Rapid polarimetric determination of bulk COF compares well with much more laborious sample-based COF measurements from thin ice sections. Because it is the former that ultimately influences ice flow, these polarimetric
15 radar methods provide an opportunity for accurate and widespread mapping of bulk COF and its incorporation into ice flow models.

1 Introduction

There is a growing need to understand the dynamics of ice sheets and how they will respond to future climate change (IPCC, 2013). The flow of ice sheets is governed by the balance between the gravitational driving stress, basal resistance to sliding,
20 and the internal deformation of ice (Cuffey and Paterson, 2010). Past flow history influences the ice crystal orientation fabric

(COF), which, in turn, influences the present-day anisotropic ice viscosity and flow field. Because ice crystals effectively re-orient themselves to minimise resistance when subjected to stress, the COF of ice is reflective of long-term strain at time scales proportional to the depth-age relationship (e.g., Alley, 1988), and has consistently been observed to align with ice deformation (Matsuoka et al., 2012). The COF of ice is also thought to be influenced by perturbations in climate on a yearly timescale

25 (Kennedy et al., 2013). Additionally, abrupt vertical changes in COF are often indicative of paleoclimatic transitions (e.g., Durand et al., 2007; Montagnat et al., 2014; Paterson, 1991). Therefore, an examination of the present-day COF can reveal past changes in the stress-strain configurations associated with historical ice flow (Brisbourne et al., 2019).

Ice core analyses represent the traditional method to quantify COF within ice sheets, and remain the only direct means of ground-truth observation. However, sites suitable for ice coring are often restricted to slow-moving ($< 50 \, \mathrm{m \, a^{-1}}$) sections of

30 ice sheets, and therefore only reveal a subset of the dynamics between ice flow and COF. These slow-flowing areas most likely do not encapsulate the dynamics and physical processes responsible for ice sheet stability and sea level rise. Furthermore, ice core analyses are often unable to resolve the absolute direction of fabric asymmetry due to the rotation of the core in the barrel during or following extraction (Fitzpatrick et al., 2014). In contrast, ice-penetrating radar offers an alternative method to calculate anisotropic COF patterns through exploiting the birefringence of polar ice without the practical limitations of drilling.

35 Although polarimetric radar sounding data analysis has been implemented to detect horizontally-asymmetric COF for almost half a century (e.g., Hargreaves, 1977), it has not yet been widely implemented, with the majority of radar studies that measure COF variations in ice being conducted within the last fifteen years at coincident ice-coring sites for comparative analysis (Drews et al., 2012; Eisen et al., 2007; Fujita et al., 2006; Jordan et al., 2019, 2020a; Li et al., 2018; Matsuoka et al., 2003, 2009, 2012). Moreover, the majority of previous polarimetric radar studies infer COF at a coarse azimuthal resolution that is

40 limited by the number of observations made along an acquisition plane that rotates around an azimuth centre (Brisbourne et al., 2019; Doake et al., 2002, 2003; Jordan et al., 2020b; Matsuoka et al., 2003, 2012). Because the maximum azimuthal resolution that can be achieved is subject to human error in measuring the angles between each acquisition plane, there is a coarse limit to the precision of the orientation of fabric asymmetry that can be achieved through this acquisition method.

Traditionally, radar studies estimated COF through power-based analyses by investigating the periodicity of birefringent

45 patterns in power anomaly (Fujita et al., 2006; Matsuoka et al., 2012) and phase difference measurements (Brisbourne et al., 2019). Recently, Jordan et al. (2019) developed a polarimetric coherence framework that extends existing methods (Dall, 2010; Fujita et al., 2006) to quantify COF eigenvalues through estimating the relative phase between orthogonal co-polarised measurements. A follow-up study by Jordan et al. (2020b) demonstrated the validity of this framework, albeit with a coarse azimuthal resolution via the azimuthal rotational setup, from measurements obtained using an autonomous phase-sensitive

50 radio-echo sounder (ApRES). The ApRES is a phase-sensitive frequency-modulated continuous-wave (FMCW) ground-based radar system (Brennan et al., 2014) that has been gaining traction over the last five years, not only to investigate englacial polarimetry (Brisbourne et al., 2019; Jordan et al., 2020b), but also in wider radioglaciological investigations involving englacial deformation (Gillet-Chaulet et al., 2011; Kingslake et al., 2014, 2016; Nicholls et al., 2015; Young et al., 2019), englacial meltwater content (Kendrick et al., 2018; Vaňková et al., 2018), basal melting (Corr et al., 2002; Davis et al., 2018; Jenkins

55 et al., 2006; Lindbäck et al., 2019; Marsh et al., 2016; Nicholls et al., 2015; Stewart et al., 2019; Sun et al., 2019; Vaňková et al., 2020; Washam et al., 2019), and subsurface imaging (Young et al., 2018).

Instead of using an azimuthal rotational setup, acquisitions can instead be obtained through a combination of four orthogonal antenna orientations, from which the received signal can then be reconstructed at any azimuthal orientation (Fig. 1a) (Fujita et al., 2006; Jordan et al., 2019). This quadrature- (quad-) polarised setup therefore resolves this limitation on azimuthal

60 resolution whilst simultaneously also significantly reducing the field time required to obtain each set of acquisitions.

In our study, we use an ApRES and two antennas to acquire a set of quad-polarised measurements at the Western Antarctic Ice Sheet (WAIS) Divide. We apply the polarimetric coherence method to these measurements to present estimates of fabric values that closely align with previous ice core COF measurements at WAIS Divide to a depth of 1500 m at a resolution of 15 m. We show that, using this setup and method, we can estimate the fabric asymmetry at resolutions at or exceeding that from

65 ice cores, and from our results unambiguously identify the principal axis of present and past flow to high angular resolution.

2 Study area

The West Antarctic Ice Sheet (WAIS) divide delineates the surface topographic boundary separating ice flow towards the Ross and Amundsen Sea Embayments (Fig. 1b). A subglacial topographic saddle runs approximately orthogonal to the ice divide in the study region. Ice flow is oriented approximately SWW (250°) and NE (45°) in the Ross and Amundsen Sea catchments

70 respectively (Conway and Rasmussen, 2009), which is offset from predicted strain configurations, especially in the Amundsen Sea catchment (Matsuoka et al., 2012). The WAIS divide flow boundary is observed to be migrating in the direction towards the Ross Sea at 10 m a^{-1}, faster than the surface velocity of 3 m a^{-1}, the migration being attributed to differential flow dynamics in the Ross Sea catchment (Conway and Rasmussen, 2009). Despite this fact, the ice-divide position has likely remained on average within 5 km of its present position throughout the Holocene epoch (Koutnik et al., 2016).

75 Our ApRES measurement site is situated approximately 20 km southeast of WAIS divide in the Ross Sea embayment. This site (79° 25′ 53″ S, 111° 59′ 15″ W, 1781 m a.s.l.) is approximately 5 km northeast of the location of the WAIS Divide deep ice core (WDC, 79° 28′ 3″ S, 112° 5′ 11″ W, 1766 m a.s.l.), which was completed to a total depth of 3405 m (~50 m above the ice-bed interface) (Fitzpatrick et al., 2014) (Fig. 1b).

3 Theory and methods

80 We primarily follow a combination of three matrix-based methods—Fujita et al. (2006), Dall (2010), and Jordan et al. (2019), in which each study builds on the previous—to process the polarimetric measurements, thereby obtaining estimates of anisotropy and fabric strength. Our approach is physically justified through an effective medium model that expresses the bulk dielectric properties of anisotropic polar ice in terms of the birefringence of individual ice crystals (Fujita et al., 2006). First, we follow the framework of Fujita et al. (2006) and Brisbourne et al. (2019) in modelling the expected power anomaly and phase difference

85 (Section 3.2) to explicate the ApRES' response to the underlying COF parameters from data collected in proximity at WAIS
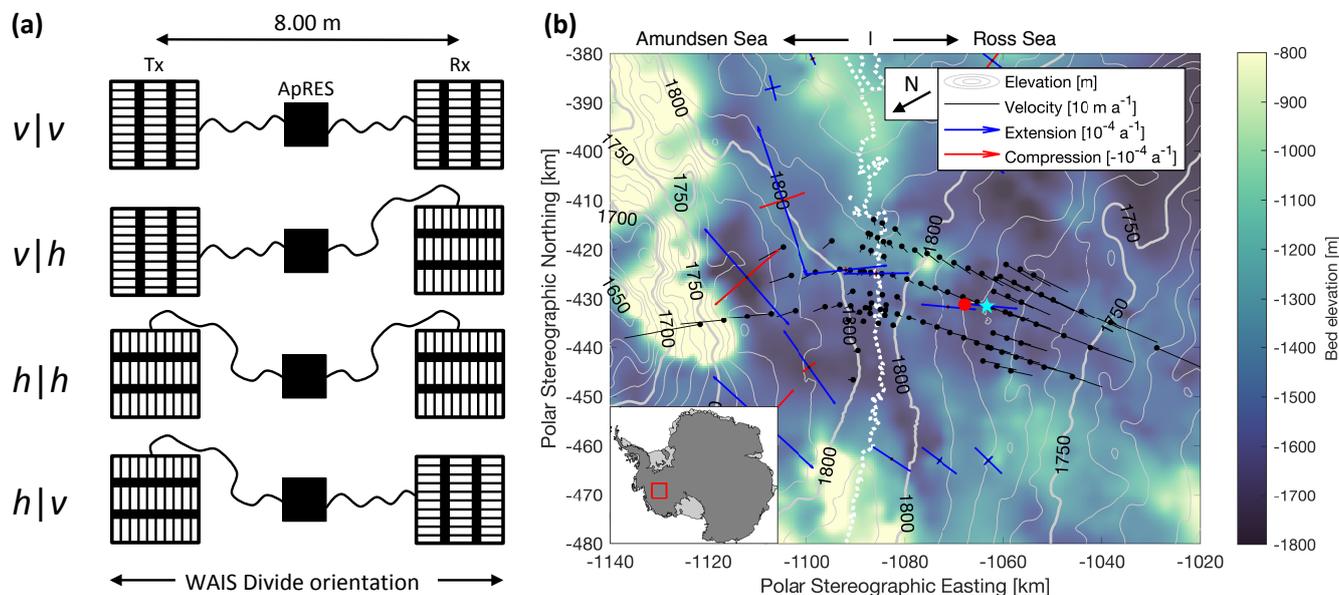
Figure 1. (a) Four orthogonal combinations of antenna orientations used for polarimetry experiments. Antennas (Tx = transmitting, Rx = receiving) were positioned 8.00 m apart and rotated 90° in a vertical (*v*) or horizontal (*h*) orientation. The antenna axis was oriented parallel with the WAIS Divide orientation. (b) Map of local surface topography (white contours, REMA, Howat et al., 2019) and bed topography (background colour, MEaSUREs BedMachine Antarctica, Morlighem et al., 2020) in the WAIS Divide area, as well as GPS-measured surface velocities (black lines, Conway and Rasmussen, 2009) and strain configurations (blue and red arrows, Matsuoka et al., 2012). The locations of the ApRES polarimetry experiment (red dot) and the WAIS Divide Deep Ice Core (WDC, cyan star) are separated by ~5 km. The WAIS Divide is delineated as a thick dotted white line, with ice flowing northwards towards the Amundsen Sea and southwards towards the Ross Sea. Location of (b) is shown as a red box in the map inset.

Divide. We then calculate the fabric asymmetry using the polarimetric coherence methods outlined in Jordan et al. (2019, 2020b).

3.1 Electromagnetic propagation and COF representation in anisotropic ice

In an anisotropic medium such as polar ice, birefringence and anisotropic scattering are two related, but separate mechanisms
90 that affect the polarisation and azimuthal variation in power of radar returns (Brisbourne et al., 2019). For downward-looking ice-penetrating radar, birefringence occurs as a result of a phase shift between two orthogonally-oriented waves travelling between the surface and the interior of an ice mass, the phase shift manifested in the radar return as characteristic variations with azimuth and depth in power and phase. As a result, birefringence reflects the bulk COF as and is azimuthally asymmetric in the direction of radio wave propagation. On the other hand, anisotropic scattering arises as a consequence of rapid but
95 microscopic continuous depth variations in the orientation of the bulk COF. Therefore, the polarimetric response of radio waves is determined by the bulk (macroscopic) birefringence of the COF (Hargreaves, 1978), of which the area illuminated by

the waves is a function of the radar antenna footprint through depth. The birefringence of an individual ice crystal and its COF are related to the bulk dielectric properties of anisotropic polar ice (Appendix of Fujita et al., 2006):

$$\varepsilon(z) = \begin{bmatrix} \varepsilon_\perp + \Delta\varepsilon E_1 & 0 & 0 \\ 0 & \varepsilon_\perp + \Delta\varepsilon E_2 & 0 \\ 0 & 0 & \varepsilon_\perp + \Delta\varepsilon E_3 \end{bmatrix} \tag{1}$$

100 where $\varepsilon(z)$ is the bulk birefringence tensor, $\Delta\varepsilon = \varepsilon_\parallel - \varepsilon_\perp$ is the crystal (microscopic) birefringence with $\varepsilon_\parallel$ and $\varepsilon_\perp$ the dielectric permittivities for polarisation planes parallel and perpendicular to the crystallographic (c)-axis. Across the spectrum of ice-penetrating radar frequencies and ice temperatures, $\varepsilon_\parallel$ and $\varepsilon_\perp$ vary within a narrow band of 3.16–3.18 and 3.12–3.14 respectively (Fujita et al., 2000). In this study, following Jordan et al. (2020b), we assign $\varepsilon_\parallel = 3.169$ and $\varepsilon_\perp = 3.134$, with $\Delta\varepsilon = 0.035$.

105   The tensor eigenvalue E describes the relative concentration of c-axes aligned with each principal coordinate eigenvector, with $E_1 + E_2 + E_3 = 1$ and $E_3 > E_2 > E_1$ following conventional radar notation, which is opposite to conventions normally in ice core studies ($E_1 > E_2 > E_3$). The relative proportions of E can be used to describe different fabric patterns, including (i) random (isotropic) fabrics ($E_1 \approx E_2 \approx E_3 \approx 1/3$); (ii) cluster fabrics ($E_1 \approx E_2 \ll E_3$); and (iii) vertical girdle fabrics ($E_1 \ll E_2 \approx E_3$). When ice deforms solely by vertical uniaxial compression, such as at the centre of an ice dome, the c-axes

110 rotates towards the vertical and forms a cluster fabric; where lateral tension exists from flow extension, such as at an ice divide, the c-axes orient in a vertical girdle distribution orthogonal to the direction of strain extension (Alley, 1988). Following previous studies (Fujita et al., 2006; Drews et al., 2012; Brisbourne et al., 2019; Jordan et al., 2019, 2020b), we assume that the E_3 eigenvector is aligned in the vertical direction, and the E_1 and E_2 eigenvectors are parallel to the horizontal plane. The direction of the greatest horizontal c-axis concentration reflects the orientation of horizontal strain extension (Brisbourne

115 et al., 2019; Matsuoka et al., 2012) and corresponds with E_2 in our notation (Jordan et al., 2020b). The E_1 eigenvector is orthogonally oriented to both E_2 and E_3, and represents the symmetry axis, which is normal to the girdle plane (Brisbourne et al., 2019).

    In the horizontal plane, Equation 1 simplifies to $\varepsilon(z) = \Delta\varepsilon(E_2 - E_1)$, where the horizontal eigenvalue difference $E_2 - E_1$ quantifies the horizontal asymmetry of the ice fabric (i.e. strength of the vertical girdle). Equation 1 directly relates both

120 the macro- and microscopic ice fabric anisotropy to dielectric anisotropy, which serves as the basis for the radar processing methods that follow.

3.2 Modelling radio-wave signal propagation

The matrix-based formulation calculates the backscatter that is transmitted, reflected, and received at the antennas for each depth step and azimuthal orientation:

125 $$S(\theta) = \left[\frac{\exp(jk_0 z)}{4\pi z}\right]^2 \cdot \left[\prod_{i=1}^{N}(RTR')_{\theta,\varepsilon,N+1-i}\right] \cdot [R\Gamma R']_{\theta,\beta,N} \cdot \left[\prod_{i=1}^{N}(RTR')_{\theta,\varepsilon,i}\right] \tag{2}$$

Equation 2 represents the polarimetric backscatter model described in Eqs. 9–12 of Fujita et al. (2006), which calculates the polarimetric backscatter for each antenna orientation combination as a function of angle (θ), anisotropy (β), and birefringence (ε), through all depth layers $z = i$ to the Nth layer. The first term on the right hand side represents the (i) free space propagation (squared to reflect two-way wave travel). Here, $j = \sqrt{-1}$ is the imaginary number, and $k_0 = 2\pi/\lambda_0 \, (\mathrm{rad\,m^{-1}})$ the wavenumber in a vacuum with λ_0 the wavelength in a vacuum. Besides the first expression, the second to fourth terms respectively represent three physical processes: (ii) received (upward) propagation; (iii) boundary scattering; and (iv) transmitted (downward) propagation to each boundary depth i. T and Γ respectively represent the transmission and scattering matrices, and R represents the rotation matrix with R' its transposition, each detailed respectively in Eqs. 5 and 6, 8, and 10 of Fujita et al. (2006), with the propagation constants required to calculate T defined specifically for the ApRES unit in Brennan et al. (2014).

3.3 Radar data acquisition

On 25 December 2019, we acquired a suite of four quad-polarimetric measurements at the study site (79° 25′ 53″ S, 111° 59′ 15″ W, 1781 m a.s.l.). These measurements were acquired using a single-input single-output (SISO) autonomous phase-sensitive radio echo sounder (ApRES; Brennan et al., 2014; Nicholls et al., 2015) that operated with a linear up-chirp from 200 to 400 MHz over the course of 1 second, corresponding to a centre frequency of 300 MHz over a bandwidth of 200 MHz. An ensemble (burst) of 100 chirps were recorded for each polarimetric measurement. Two open-structure antennas (1 transmitting and 1 receiving) identical to those described in Nicholls et al. (2015) were used to transmit and receive each burst. Although not implemented in this study, we note that the four quad-polarimetric measurements can potentially also be obtained simultaneously in one single burst using a multiple-input multiple-output (MIMO) configuration (e.g., Young et al., 2018) with two transmitting and two receiving antennas.

The quad-polarimetric measurements represent the combination of orthogonal antenna orientations, where antennas were positioned in either a horizontal (h) or vertical (v) alignment with respect to the acquisition geometry. The four orientations that correspond to the four polarimetric measurements are therefore (i) hh, (ii) vh, (iii) hv, and (iv) vv, the nomenclature reflective of the transmitting and receiving antenna in respective order (Fig. 1a). Measurements were conducted sequentially, and each antenna pair orientation was established simply by rotating one or both antennas by 90° with respect to their previous orientations while keeping the position of each antenna centre constant. In our experiment, the v-polarisation plane was aligned to the southwest (250°).

3.4 Radar data processing

Data were pre-processed and range-processed following procedures detailed in Stewart et al. (2019). Specifically, for each of the four bursts, the 20 noisiest chirps were culled and the remaining chirps averaged. Each resulting burst-mean was then weighted with a Blackman window, zero-padded, time-shifted to align the phase centre with the start of the signal, and Fourier-transformed. The resulting complex-valued spectra (referred to as complex amplitude) store the amplitude and the phase of the signal as the magnitude and the angle of the spectra respectively.

Using the four processed quad-polarised complex amplitudes, the 2×2 integrated scattering matrix S (Eq. 2) in the frame of reference can be constructed as (Doake et al., 2003):

$$S = \begin{bmatrix} s_{hh} & s_{vh} \\ s_{hv} & s_{vv} \end{bmatrix} \tag{3}$$

Equation 3 is often referred to as the Sinclair matrix. From here, we can reconstruct the ApRES received signal S from any transmission angle through the application of an azimuthal (rotational) shift of principal axes at the transmitting and receiving antennas (e.g., Mott, 2006):

$$
\begin{aligned}
S(\theta) &= \begin{bmatrix} \cos\theta & \sin\theta \\ -\sin\theta & \cos\theta \end{bmatrix} \begin{bmatrix} s_{hh} & s_{vh} \\ s_{hv} & s_{vv} \end{bmatrix} \begin{bmatrix} \cos\theta & -\sin\theta \\ \sin\theta & \cos\theta \end{bmatrix} \\
&= \begin{bmatrix} s_{hh}\cos^2\theta + (s_{vh}+s_{hv})\sin\theta\cos\theta + s_{vv}\sin^2\theta & s_{hv}\cos^2\theta + (s_{vv}-s_{hh})\sin\theta\cos\theta - s_{vh}\sin^2\theta \\ s_{vh}\cos^2\theta + (s_{vv}-s_{hh})\sin\theta\cos\theta - s_{hv}\sin^2\theta & s_{vv}\cos^2\theta - (s_{vh}+s_{hv})\sin\theta\cos\theta + s_{hh}\sin^2\theta \end{bmatrix}
\end{aligned} \tag{4}
$$

Note that in Eq. 4 the cross-polarised measurements obtained from the ApRES are geometrically congruent by the Lorentz Reciprocity Theorem (i.e. $s_{vh} = s_{hv}$) and therefore the two measurements should be identical, with any deviations being the result of performance variations between the transmitting and receiving antennas and/or error in orienting the antennas along the acquisition geometry axes (Doake et al., 2003).

Because the complex amplitudes retrieved from the ApRES (Eq. 4) are phasors representing the radar return signal, the phase of the signal at a given depth is simply the argument of the complex number. To avoid the typical problems of working with phase—that is, employing phase unwrapping methods for sampled data within $[0, 2\pi]$—we calculate the phase difference with respect to azimuth:

$$\Delta\phi_{\theta,z} = \arg\left(s_{\theta+\Delta\theta/2,z} \cdot s^*_{\theta-\Delta\theta/2,z} \right) \tag{5}$$

where the asterisk represents the complex conjugate of its respective phasor.

The shift in phase also results in the modulation of received power as a function of azimuth. This can be visualised by calculating the power anomaly from the resulting multipolarisation data (e.g. Eq. 7 in Matsuoka et al., 2003).

The polarimetric coherence and its corresponding phase is computed over a local window via the discrete approximation (Eq. 1 in Dall, 2010):

$$c^\star_{hhvv} = \frac{\sum_{i=1}^{N} s_{hh,i} \cdot s^*_{vv,i}}{\sqrt{\sum_{i=1}^{N} |s_{hh,i}|^2}\sqrt{\sum_{i=1}^{N} |s_{vv,i}|^2}} \tag{6a}$$

$$\phi^\star_{hhvv} = \arg\left(c_{hhvv} \right) \tag{6b}$$

where the superscript stars in Eq. 6 account for the use of the deramped phase stored by the ApRES rather than the original received signal phase (hereafter we do not notate this explicitly) (Jordan et al., 2020b). From Eq. 6b, we can then estimate the

fabric asymmetry of the underlying ice column $E_2 - E_1$ by (Eqs. 22 and 23 in Jordan et al., 2019):

185
$$E_2 - E_1 = \frac{c}{4\pi f_c} \frac{2\sqrt{\varepsilon}}{f(\nu)\Delta\varepsilon} \left| \frac{d\phi_{hhvv}(\alpha = 0°, 90°)}{dz} \right| \tag{7a}$$

$$\frac{d\phi_{hhvv}}{dz} = \frac{R\frac{dI}{dz} - I\frac{dR}{dz}}{R^2 + I^2} \tag{7b}$$

with the associated phase error was estimated through the Cramér-Rao Bound, following the methods of Jordan et al. (2019). In Eq. 7b, R and I respectively represent the real and imaginary components of c_{hhvv}. $f(\nu)$ represents a reduction parameter for the birefringence of firn with respect to solid ice, with ν the firn density, as detailed in the Appendix of Jordan et al. (2020b).

190 Firn densities from Fig. 9a of Gregory et al. (2014) were used as values of ν. The presence of $f(\nu)$ into Eq. 7a amplifies the estimated $E_2 - E_1$ values for the top ~100 m of the ice column.

4   Results

Figure 2 shows the processed results from the ApRES polarimetry experiment. A pad factor of 2 (equating to a depth resolution of 0.27 m) and an azimuthal resolution of $1°$ was used in the phase processing steps to produce co- and cross-polarised profiles

195 of power anomaly and phase difference (Fig. 2b,c,d). A depth window of 15 m was used in the $hhvv$ coherence and phase estimates (Fig. 2e). We evaluated $d\phi_{hhvv}/dz$ and estimated its respective error following the suggested procedures in Jordan et al. (2019), with the exception that, in substitution of the FIR filter, we used a 2-D median filter consisting of a $1° \times 5$ m matrix moved over the profile, and then a 2-D peak convolution using a Gaussian low-pass filter with the same moving matrix dimensions (Young et al., 2018). We compare the measured results in Fig. 2 with modelled results in Fig. 3 to parse the relative

200 influence of birefringent propagation and anisotropic scattering on the ice column. From here, we estimate fabric asymmetry via Eq. 7a to solve for $E_2 - E_1$ (Fig. 4). We restrict our observations only to measurements with sufficiently high signal-to-noise ratios (SNR). We also do not make any inferences in the uppermost 20 m due to potential radiation pattern effects.

The depth-azimuth variation of the radar return power anomaly in the co-polarised and cross-polarised measurements are respectively shown in Fig. 2b and Fig. 2c, variations in the co-polarised return signal phase difference in Fig. 2d, and varia-

205 tions in the $hhvv$ phase angle in Fig. 2e. Here, we observe azimuthal variations larger than 10 dB in the observed backscatter power both in the co-polarised and cross-polarised measurements, and variations larger than 6 dB in the $hhvv$ phase measurements. The backscatter variations in the co-polarised power anomaly (Fig. 2b) and $hhvv$ phase measurements (Fig. 2e) show reflectional symmetry at $90°$ at all measured depths in our experiment reference frame. The co-polarised phase difference measurements (Fig. 2d) show characteristic 'four-quadrant patterns' formed by azimuthal rotation of the phase-difference

210 sign reversals (Brisbourne et al., 2019) along the same reflection axis. The cross-polarised power anomaly measurements, in contrast, show a $90°$ periodicity in the return power difference with a depth-constant azimuthal minima at $0°$ and $90°$ (Fig. 2c). By tracing the azimuthal minima in the cross-polarised power anomaly profiles through depth (Fig. 2c) (Li et al., 2018) and resolving the observed $90°$ ambiguity by identifying the azimuthal location of the centre of the quadrant patterns (Fig. 2b) (Brisbourne et al., 2019), we can identify the orientation of the symmetry axis. In this way, we identify the minima in return

215 power difference along the symmetry axis at $90°\pm7°$ (standard error), corresponding to a southwesterly $(250°)$ flow direction.
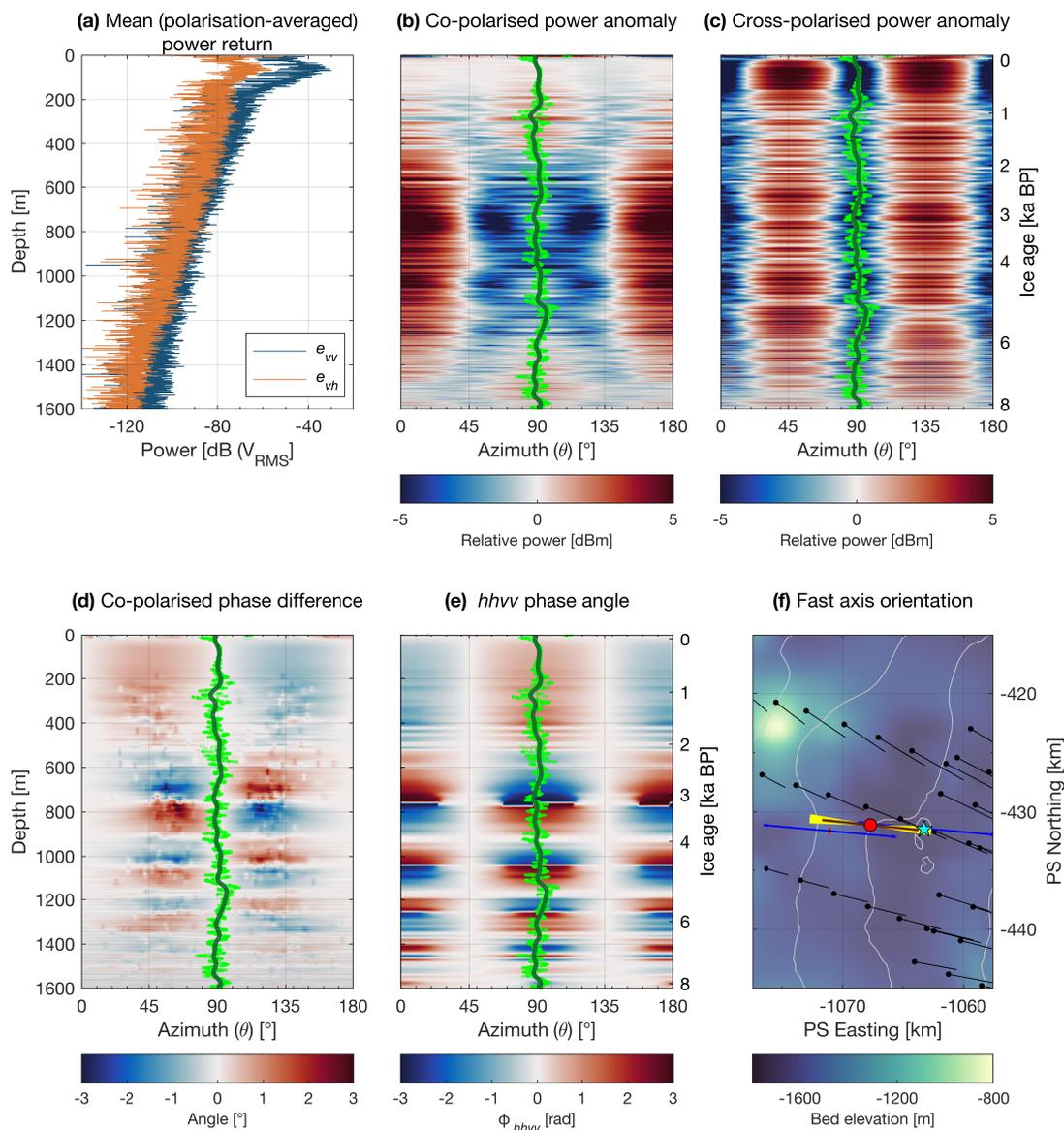
Figure 2. Polarimetric power and coherence measured using ApRES at WAIS Divide. (a) Mean (polarisation-averaged) power return. (b) Co-polarised and (c) cross-polarised power anomaly. (d) Co-polarised phase difference. (e) Quad-polarised ($hhvv$) phase angle. (f) Orientation of the principal axis (dark brown) and associated standard error (yellow bounds) as determined from the E_2 eigenvector in (c). Depths with insufficient SNR (primarily > 1500 m) are greyed out. Bright green dots represent azimuthal minima at each range bin after zero-padding (0.27 m), The dark green line is the best estimate of the symmetry axis, calculated using a Gaussian-weighted moving average of the azimuthal minima. The depth-dependent gradient along the symmetry axis represents $E_2 - E_1$, the fabric asymmetry of the measured vertical ice column. Map shown in (f) is an inset of Fig. 1b.
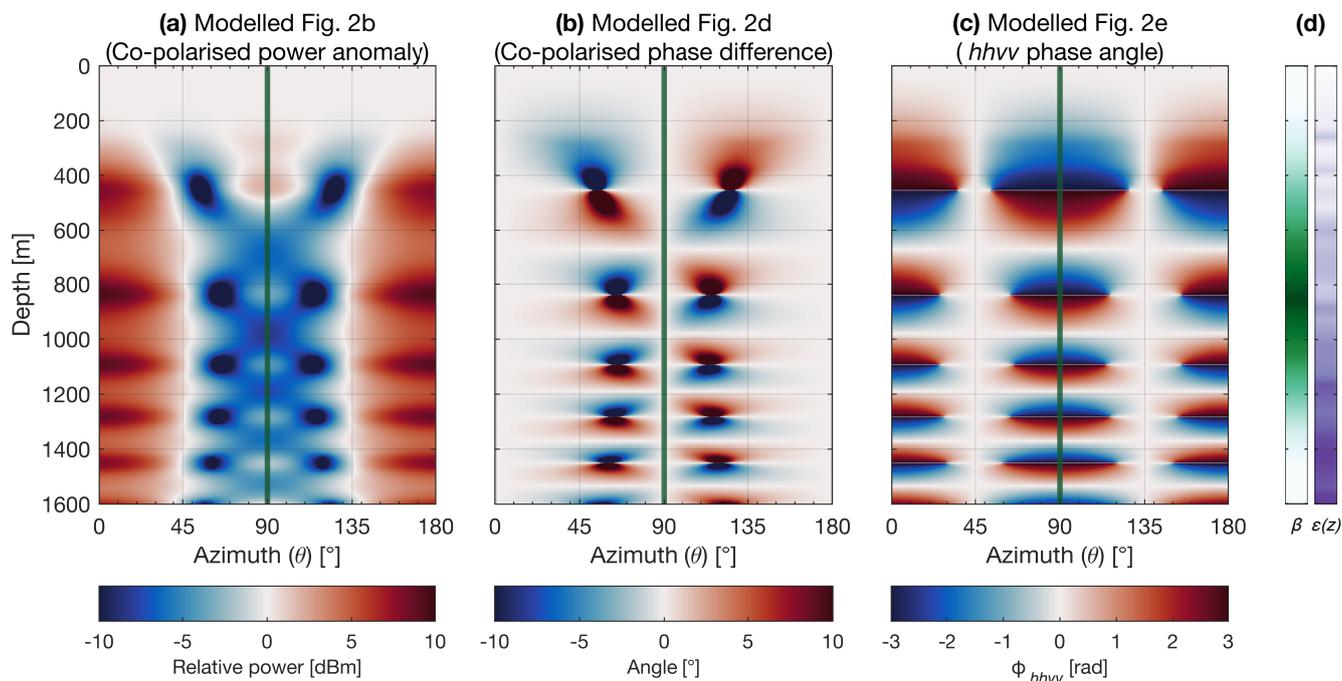
Figure 3. Modelled WDC (a) co-polarised power anomaly, (b) co-polarised phase difference, and (c) quad-polarised ($hhvv$) phase angle, corresponding to Fig. 2b, d, and e respectively. (d) Model input parameters for anisotropy (β), and birefringence ($\varepsilon(z)$) through depth, the former estimated through 2-D optimisation from Fig. 2b, and the latter using eigenvalues from the WDC that specify the bulk COF (Fitzpatrick et al., 2014). Value ranges for β (white to dark green) and $\varepsilon(z)$ (white to dark purple) are $[1\ 5]$ and $\left[0\ 1.5 \times 10^{-2}\right]$ respectively.

The identified symmetry axis orientation does not azimuthally migrate through the observed depth range to $1500\,\mathrm{m}$, equivalent to a depth age of 7400 years (Sigl et al., 2016). Though we similarly observe no azimuthal migration beyond $1500\,\mathrm{m}$, we do not extend our findings further due to the limited depth samples with sufficient SNR available within this range. Our estimate of the principal axis aligns exactly with the nearest strain configuration (~5 km southwest) as estimated by Matsuoka et al.

220 (2012), and is $+14°$ from the direction of flow as estimated by Conway and Rasmussen (2009) (Fig 2f). We note that there may be additional unquantified azimuthal error from human inaccuracy in establishing the orientation of the measurement axis during data collection.

The backscatter and phase patterns in the co-polarised measurements, as well as in the $hhvv$ coherence phase (ϕ_{hhvv}), all show variation with depth, which indicate changes in either or a combination of birefringence and anisotropy. To better under-

225 stand what drives these changes, we modelled the azimuth and phase dependence of these three measurements (Fig. 3) through the matrix-based backscatter model (Eq. 2), which predicts the combined polarimetric effect of birefringent propagation and anisotropic scattering at each depth and azimuth step ($1\,\mathrm{m}$ and $1°$ in the model). The birefringence in the models was estimated through Eq. 1 by directly using eigenvalue estimates from the WAIS Divide Deep Ice Core (WDC; Fitzpatrick et al., 2014) to calculate the horizontal asymmetry $E_2 - E_1$, and linearly interpolating between each defined fabric measurement depth. The

230 eigenvalues from the ice core analysis suggest a gradual linear transition from an isotropic fabric ($E_2 - E_1 \approx 0.04$) near the ice surface to a moderately-strong girdle fabric ($E_2 - E_1 \approx 0.3$) at 1500 m depth (Fig. 4). As the principal axis observed in the polarised experiment is depth-invariant, we fixed the principal axes at $90°$ following our observations in Fig. 2c. The remaining parameter, anisotropy, was simply estimated as an optimisation problem through identifying the azimuthal distance of nodes (minima) in power anomaly from the principal axis orientation at 100 m depth intervals. At each depth interval, the anisotropy

235 parameter β was estimated to the nearest integer and linearly interpolated to match the model depth step of 1 m.

The model outputs for the co-polarised power anomaly and phase difference, as well as the $hhvv$ phase angle cases are shown in Fig. 3, and reinforces the observations of Brisbourne et al. (2019), where characteristic "node pairs" in the minima of the power anomaly (Fig. 3a) are coincident with the four-quadrant vertical pair centres in the co-polarised phase difference (Fig. 3b). These centres are also coincident with the width of the asymptotic zone of similarly alternating positive and negative

240 phase gradients in the $hhvv$ coherence phase plot (Fig. 3c) (Jordan et al., 2019). Additionally, in Fig. 3a, cruciate-shaped zones of power minima link each node pair diagonally. In all three panels, the nodes and inflexion points are either reflectionally (Fig. 3a,c) or rotationally symmetric (Fig. 3b) around the $90°$ principal axis. The azimuthal distance of these nodes, centres, and the width of the asymptotic zones from the principal axis are a function of anisotropic scattering (Fig. 3d) that we do not consider in this study, the reasons behind elaborated in the Discussion (Section 5). The depth-periodicity of pattern repetition

245 is a function of birefringence, interpreted in past observations (e.g., Brisbourne et al., 2019; Drews et al., 2012) as a radar-measured phenomenon that arises as a consequence of bulk COF (Fig. 3d).

Several minor differences observed between the measured and modelled results include: (i) a scalar reduction in the overall ranges of power anomaly and phase difference values; (ii) the absence of the upper half of the shallowest phase reversal in the measured co-polarised phase difference and phase angle profiles (Fig. 2d,e); (iii) an offset in pattern repetition (e.g., nodes,

250 quadrants, phase reversals) that increases in depth; and (iv) an absence of noticeable patterns in the shallowest 200 m of the vertical ice column. Notwithstanding these differences, model results in Fig. 3 overall match their counterparts in Fig. 2b, d, and e to a high degree. With the exception of (ii), the corresponding locations and sizes of nodes in the power anomaly, quadrants in the phase difference, and asymptotic zones predicted by the model can all be observed in the measured results at 200–1500 m. Observations below 1500 m depth remain inconclusive, due to the low SNR present at this depth range (Fig. 2a).

255 Estimates of $E_2 - E_1$, a measure of fabric asymmetry, were made by calculating the depth-dependent gradient of the hhvv phase difference along the symmetry axis (Fig. 2e) at each 15-m depth window to obtain $d\phi_{hhvv}/dz$ (Eq. 7b), and are shown alongside equivalent $E_2 - E_1$ measurements from the WDC (Fig. 4). We do not calculate $E_2 - E_1$ in the uppermost 20 m due to the antennas being subjected to near-surface non-axisymmetric antenna radiation pattern effects. Overall, fabric asymmetry estimates from ApRES match well to WDC ice core estimates, especially between 600–1200 m, where the mismatch between

260 the two depth series averaged less than 0.02. When comparing the two independently-calculated fabric asymmetry datasets at the discrete depths at which the ice core thin sections were extracted from, the resulting correlation was moderately high between 600–1200 m ($r^2 = 0.55$), and slightly lower over the entirety of the depth series overlap to 1500 m ($r^2 = 0.45$). Both datasets show a general increase in $E_2 - E_1$ with increasing depth, with ApRES fabric measurements overall showing more variability than estimates from the WDC along their respective trends. The one exception to this positive correlation occurs
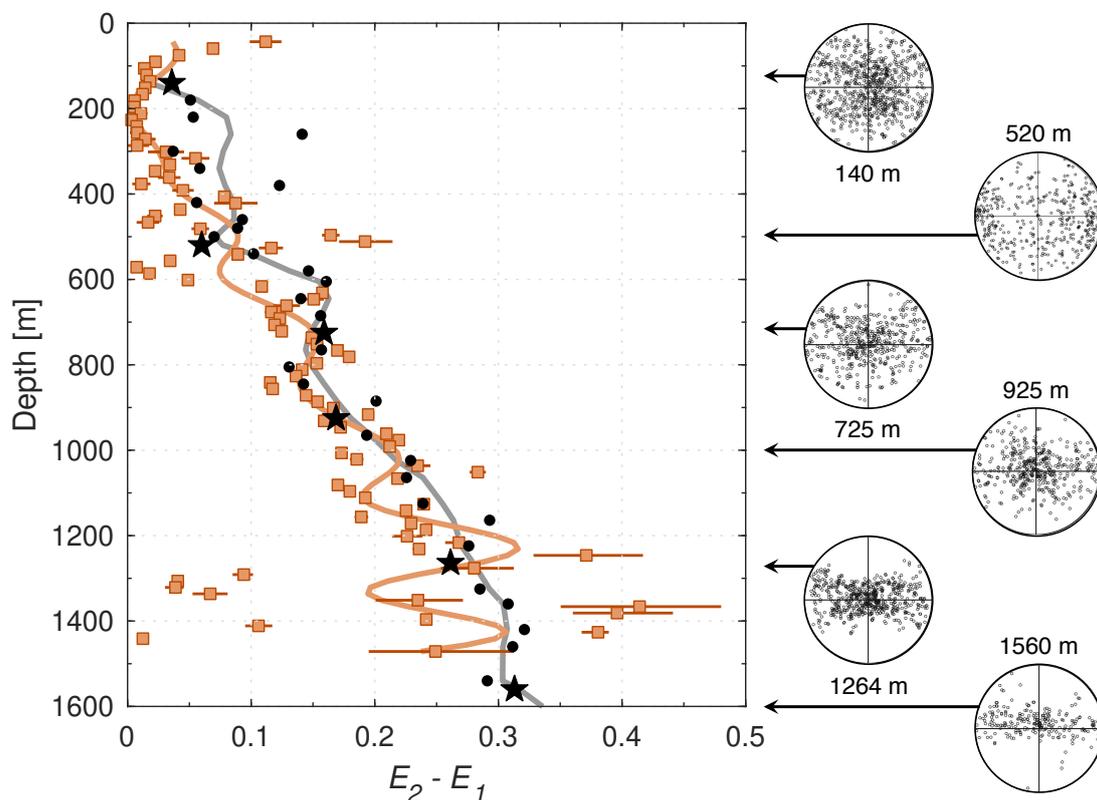
Figure 4. Modelled $E_2 - E_1$ values derived from the ApRES experiment (orange squares, with associated standard errors) and from the WAIS Divide deep ice core (black dots, Fitzpatrick et al., 2014). Smoothing curves were generated through a low pass filter on each dataset are shown in their respective colour scheme. A representative selection (black stars) of horizontal Schmidt plots from which the fabric eigenvalues for the WAIS Divide deep ice core were derived from are displayed to the right of the graph (Fitzpatrick et al., 2014).

265   between 100 and 400 m, where a small decrease in fabric asymmetry with depth can be observed in the uppermost 100 m of the ice column, where upon reaching minimum values at 200 m, rebound and show a linear increase beyond this depth. From 1200 to 1500 m, ApRES measurements show a marked increase in variability that, although centred around corresponding depth values in the WDC, varied between 0.04 to 0.42. We similarly observe a sevenfold jump increase in the associated standard error, ranging from values averaging 0.006 at depths of 200–1200 m to 0.04 within the depth range of 1200–1500 m. We do

270   not calculate $E_2 - E_1$ from the ApRES record beyond 1500 m due to low SNR in this range (Fig. 2a).

5 Discussion

5.1 Competing influences between anisotropy and birefringence

The azimuthal dependency of backscattered power in ground-penetrating radar is a function of both anisotropic scattering and birefringence (Hargreaves, 1977). Although these two terms are related, they manifest from different electromagnetic phenom-
275 ena. The birefringent propagation of radio waves arises from differences in dielectric permittivity along two axes perpendicular to the propagation direction, the two axes often referred to as the fast and slow axes or the ordinary and extraordinary axes. On the other hand, anisotropic scattering is a consequence of changes with depth in the anisotropy of permittivity in ice crystals that may not necessarily be related to changes in crystal orientation fabric (COF) (Drews et al., 2012). Both phenomena often occur simultaneously, but our technique focuses on the analysis of the birefringent signals, which provides information on the
280 bulk COF (Brisbourne et al., 2019).

Past analyses (Brisbourne et al., 2019; Fujita et al., 2006) have qualitatively inferred COF through identifying the depth-periodicity of both the node-pair minima in the co-polarised power anomaly measurements and the quadrant centres in the co-polarised phase difference measurements—in other words, the more closely spaced the nodes and quadrants are in depth, the stronger the fabric asymmetry. The periodicity of these phenomena is a manifestation of the crystal birefringence as identified
285 by the received radio-wave signal (Eq. 1). In this study, we extended the qualitative analyses suggested by these previous studies to obtain quantitative measurements of the fabric asymmetry at WAIS Divide via the polarimetric coherence method (Jordan et al., 2019), and show that the results gleaned from qualitative analyses are compatible with quantitative $E_2 - E_1$ fabric asymmetry values.

The power anomaly model that best matches observed results (Fig. 3a) incorporated a variable anisotropic parameter, which
290 predicted an isotropic medium at depths above 200 m and below 1500 m, and an anisotropic medium between these two bounds with a maximum scattering anomaly of 5 dB observed at 850 m (Fig. 3d). Drews et al. (2012) also observed azimuthal variations in backscatter power anomaly that varied similarly through depth, the variations which they attributed to micro-scopic (sub-metre) depth transitions in COF. The study also observed the superimposition of elongated bubbles that varied similarly with depth. While the induced polarimetric dependence through these bubbles was calculated to be minimal, where
295 microscopic vertically-varying COF dominates the observed anisotropy, this effect was observed to be amplified at shallower depths. Although we calculate COF in our analysis, we cannot confirm the mechanisms for the observed anisotropy in our results, as the COF values represent not only a bulk-depth average within the calculated depth bin but also a manifestation of the horizontal rather than vertical asymmetry. Interestingly, however, we note that the anisotropic zone parsed from the ApRES measurements (~400–1200 m) coincides almost exactly with the brittle ice zone (650–1300 m, Fitzpatrick et al., 2014), the
300 bubble-clathrate zone (700–1250 m, Fitzpatrick et al., 2014), and the zone where bubble shapes were least-equant (400–1500 m, Fegyveresi et al., 2016). Although these correlations warrant further investigation, they are all outside the scope of our study. Rather, we focus our analysis on the observed bulk birefringence that arises as a result of the observed COF asymmetry.

Our method applies density-dependent firn correction as suggested by Jordan et al. (2020b), which effectively reduces the value of $\Delta\varepsilon$ by taking into account the birefringence of firn with respect to solid ice, which in turn increase the fabric asymmetry

305 $E_2 - E_1$. We observe slight anisotropy of fabric that is most apparent in the uppermost 100 m of the ice column that is inversely proportional to depth. As the quad-polarisation measurements were conducted using a ground-based monostatic antenna setup, we are able to discount the possibility of a tilt angle between the E_3 eigenvector and the direction of radio wave propagation being the source of this observed firn asymmetry (Jordan et al., 2019; Matsuoka et al., 2009). On the other hand, crystal anisotropy in snow (Calonne et al., 2017) and firn (DiPrinzio et al., 2005; Fujita et al., 2009) have previously been observed on

310 multiple occasions, and is thought to be induced by perturbations in climate such as temperature, solar radiation, winds, and deposition, where the combined effects of these variables influence the initial orientation and size of ice crystals (Kennedy et al., 2013), potentially amplifying the resulting ice flow dynamics (Wang et al., 2018). While we cannot at this point conclusively link the observed fabric asymmetry in the uppermost 200 m of the ice column to climate perturbations, it is certainly a plausible explanation especially given increasingly volatile climatic conditions over the Western Antarctic Ice Sheet over the past century

315 that will likely intensify in the near future (Nicolas and Bromwich, 2011; Scott et al., 2019).

5.2 Flow history at WAIS Divide

With the addition of our ApRES-derived dataset, there are now three calculations of ice fabric at WAIS Divide. Each dataset was obtained using independent methods, with the other two arising from ice core observations (Fitzpatrick et al., 2014) and sonic logging (Kluskiewicz et al., 2017). A fourth method, observed from shear-wave splitting in seismic surveys, was conducted

320 in the 2018 summer at WAIS Divide and results gleaned from this seismic experiment (Nakata et al., *in prep*) would likely complement observations made from the corresponding datasets as an additional independent experiment.

We also note that an areal radar polarimetric study was conducted at WAIS Divide by Matsuoka et al. (2012), which quantified the relative orientation of the fabric asymmetry across a 60 km $\times$ 150 km study area, but stopped short of calculating the COF structure within their polarimetric measurements. Across the study area, they observed depth-variable azimuthal shifts

325 that varied according to the strain regime at the corresponding age-depth period. At the WDC (their S-W24), however, their results were inconclusive due to the multiple unevenly-spaced azimuthal power maxima at depth in both radar frequency returns. Our results contrast with those of Matsuoka et al. (2012) in that we observe no azimuthal ambiguity in our determination of the symmetry axis down to a depth of 1500 m, which translates to a depth-age of ~7400 years BP (before 1950), which encompasses the majority of the Holocene epoch. The depth-age of the record is short because the rates of accumulation over

330 this time period are high in comparison to both historical rates over the same area (Fudge et al., 2013) and present-day rates over other areas across the Antarctic Ice Sheet (Koutnik et al., 2016). Therefore, given that our ApRES measurement location is situated within 20 km from the present-day location of WAIS Divide, our observations of a depth-invariant symmetry axis is consistent with the proposition that the ice divide has likely remained on average within 5 km of its present position throughout the Holocene (Koutnik et al., 2016).

335 ### 5.3 Method comparisons and limitations

Jordan et al. (2019) puts forth the advantage of using polarimetric radar methods to determine the orientation of fabric, especially with regards to the fact that ice core studies can only be conducted in a relative azimuthal reference frame due to the

rotational spin of the core during the drilling process. Our study confirms this proposition by establishing the orientation of the symmetry axis through the identification of depth-local minima in the cross-polarised power anomaly measurements (Fig. 2c).

340 Although the cross-polarised power anomaly has a 90° ambiguity (Li et al., 2018), this ambiguity can be resolved if the corresponding co-polarised measurements detect anisotropic scattering (Brisbourne et al., 2019). We find that the symmetry axis orientation observed in our measurements aligns exactly with the observed present-day surface strain regime rather than the orientation of flow, at 250°±7° (Fig. 2f), consistent with theory relating ice flow and crystal anisotropy (Azuma, 1994).

Of the methods available to quantify depth changes in ice COF, only ice core analyses are currently able to produce a fully

345 three-dimensional set of fabric estimates. Thin (~10 cm) section analyses from ice cores, while providing direct orientation estimates for the majority of grains within each section, are often conducted at depth intervals of tens of metres, with each analysis capturing the local decimetre-wide fabric regime, as is the case for the WAIS Divide deep ice core (WDC) at an average depth interval of 40 metres (Fitzpatrick et al., 2014). In contrast, waveform-based methods average out fabric properties in bulk where, for radar systems, the planar footprint of which the COF is averaged from is dependent on the radiation patterns

350 of the radar antennas and increases linearly through depth, and can be approximated as the radius of the first Fresnel zone (Haynes et al., 2018). As the antennas used in this study have a relatively wide half-power beamwidth (±30°), the footprint of the ApRES system would have a radius of approximately 1/4 of the centre wavelength (~1 m) near the surface, but reaches to approximately 1000 m at a depth of 1500 m. Therefore, the bulk COF estimates obtained from ApRES is averaged from a much larger area at depth than near the surface. Along with the SNR, this observed scale-dependence would therefore heavily

355 influence the accuracy and error of results, especially in areas of complex flow and deformation.

The COF resolution vary significantly between waveform-based methods. For example, seismic surveys generate high azimuthal resolution at the cost of depth resolution (e.g., Horgan et al., 2011; Brisbourne et al., 2019), while equivalent results from sonic logging techniques reveal the converse (e.g., Gusmeroli et al., 2012; Kluskiewicz et al., 2017). While bulk-averaging over a large amount of crystals induces higher amounts of statistical noise compared to thin-section analysis, they are better

360 able to resolve smaller scale features and discontinuities in the observed fabric (Wilen et al., 2003). Our results using a phase-sensitive radio echo sounder, while reconstructed from orthogonal measurements, offer a compromise between azimuthal and depth precision, providing COF estimates comparable to results from the WDC at resolutions comparable to that of seismics in azimuth and sonic logging in depth.

The use of quad-polarised measurements is depth-limited by the signal-to-noise ratio of the cross-polarised terms (s_{hv} and

365 s_{vh}). Our COF measurements obtained from polarimetric radar, where chirps were coherently summed during pre-processing for each measurement, correlate well with equivalent ice-core measurements made at WDC to a depth of 1500 m, after which the phase is dominated by noise. Given that the relative power of the cross-polarised terms are almost a magnitude lower than that of the co-polarised terms (Fig. 2a), accurate COF calculations using ApRES most likely can not exceed this depth limit with the current specifications.

370 As this study and those by Jordan et al. (2019, 2020b) show, the polarimetric coherence method measures the horizontal asymmetry of the vertical ice column through quantifying the birefringence effects from orthogonally-oriented measurements and relating this to the difference in magnitude between the E_2 and E_1 eigenvectors. As such, an obvious limitation of this

method is its inability to discern azimuthally-invariant fabric such as single-cluster crystal distributions or more complex fabrics
such as horizontal girdles from each other. However, given the high resolution of the results, ApRES-derived COF are directly
375 complementary to results from sonic logging in that the former calculates the horizontal asymmetry of the fabric through
quantification of $E_2 - E_1$, whilst the latter quantifies the vertical fabric asymmetry (the strength of the E_3 eigenvector) through
P-wave interpretation (Kluskiewicz et al., 2017).

An obvious advantage of seismic and radar surveys, in comparison to ice coring and sonic logging, is that they can be
implemented as a much smaller operation in terms of team size, cost, and field time, with ground-based radar surveys an
380 order of magnitude even lower than that of seismics and airborne radar in all three aspects. As a reference, the quad-polarised
measurements collected in this study took approximately thirty minutes inclusive of radar and antenna setup, and involved
only two persons (co-authors Young and Dawson). While radar surveys can be conducted efficiently in comparison to that
of seismics surveys, the latter is able to estimate COF in three dimensions (albeit with a vertically-integrated value) and can
distinguish azimuthally-symmetric forms of anisotropy that the former at present cannot. A combination of these two methods
385 can therefore reduce ambiguity in fabric estimation (Brisbourne et al., 2019), especially in areas of complex flow which have
the potential to produce complex fabric. Additionally, these methods have the ability to measure COF in a wide variety of flow
regimes that may not be suitable as an ice core drilling site. In this respect, the use of one or a combination of geophysical
methods has the potential to investigate more dynamic areas that reveal the complexities of ice flow, such as shear margins or
grounding zones. In conclusion, as shown in our study, the use of an ApRES in conjunction with the polarimetric coherence
390 method can produce estimates of fabric asymmetry with accuracies comparable to and resolutions exceeding that of thin ice
core section analyses.

6 Conclusions

Using a phase-sensitive radar and two open-structure antennas, we conducted a suite of quadrature-polarimetric measurements
within the proximity of the WAIS Divide Ice Core (WDC). Using a combination of the matrix-based backscatter model (Bris-
395 bourne et al., 2019; Fujita et al., 2006) and the polarimetric coherence method (Jordan et al., 2019, 2020b), we were able to
(i) quantify the horizontal asymmetry ($E_2 - E_1$) of the crystal orientation fabric (COF) to a depth of 1500 m; and (ii) unam-
biguously identify the fabric asymmetry to be depth invariant with the symmetry axis oriented at $250°\pm7°$ to the same depth
of 1500 m. Our findings in (i) were conducted at an angular and vertical resolution of $1°$ and 15 m respectively, exceeding that
of ice core-derived measurements made at the WDC (Fitzpatrick et al., 2014). The correlation between these two independent
400 measurements of fabric asymmetry is moderately high over the depth range of 600–1200 m ($r^2 = 0.55$), and is slightly lower
over the entire depth range to 1500 m ($r^2 = 0.45$). Our findings in (ii) align exactly with the direction of principal strain in-
dependently measured by Matsuoka et al. (2012). Our determination of depth-invariant fabric orientation to at least 1500 m,
equivalent to 7400 years BP (years before 1950), covers ~65% of the Holocene epoch, which suggests that the deformation
regime at WAIS Divide has not changed substantially during this period. While ice core-based measurements still represent
405 the only method that is able to estimate COF in three dimensions, the logistics required to conduct polarimetric radar mea-

surements to quantify fabric asymmetry are minimal and non-invasive. In this regard, polarimetric radar methods provide an opportunity for accurate and widespread profiling and mapping of bulk COF across a diverse range of flow regimes, with the potential to illuminate the role of fabric asymmetry on ice rheology.

Code and data availability. The full set of ApRES polarimetric measurements and associated processing code will shortly be made available
410 through the UK Polar Data Centre (https://www.bas.ac.uk/data/uk-pdc/) shortly after this manuscript is published. Until that time, these data are available by request from the corresponding author.

Author contributions. TJY designed the polarimetric experiment with assistance from CM, who wrote the polarimetric backscatter model. TJY and EJD collected the ApRES data as part of the TIME project within the International Thwaites Glacier Collaboration. TJY processed the ApRES data, analysed the results, and wrote the manuscript with guidance from CM. All authors contributed to manuscript preparation.

415 *Competing interests.* The authors declare that they have no conflicts of interest.

Acknowledgements. This research is an output from the Thwaites Interdisciplinary Margin Evolution (TIME) project as part of the International Thwaites Glacier Collaboration (ITGC), which include the UK Natural Environment Research Council (NERC) research grant #NE/S006788/1 supporting T. J. Young and Poul Christoffersen, and the USA National Science Foundation (NSF) research grant #1739027 supporting Slawek Tulaczyk and Dustin Schroeder. Eliza Dawson is supported by an NSF Graduate Research Fellowship. We appreciate
420 logistical support from the 2019/20 station leader (James King) and staff at WAIS Divide Field Camp, as well as aviation support from the United States Air National Guard and Kenn Borek Air during our field season. We thank Jake Walter, Stephen Veitch, Forrest McCarthy, and Julie Baum as fellow team members in our field season. We thank all members of the ITGC TIME project for insightful discussions on waveform analysis, ice fabric, and anisotropy. We similarly thank Keith Nicholls for insightful discussions as well as loaning the ApRES unit at short notice. We are also grateful to Howard Conway for providing GPS-measured velocity data to contextualise our results. Associated
425 data and code will be made available in line with the policies outlined by the ITGC.

References

Alley, R. B.: Fabrics in polar ice sheets: Development and prediction, Science, 240, 493–495, https://doi.org/10.1126/science.240.4851.493, 1988.

Azuma, N.: A flow law for anisotropic ice and its application to ice sheets, Earth and Planetary Science Letters, 128, 601–614,
430 https://doi.org/10.1016/0012-821X(94)90173-2, 1994.

Brennan, P. V., Nicholls, K. W., Lok, L. B., and Corr, H. F. J.: Phase-sensitive FMCW radar system for high-precision Antarctic ice shelf profile monitoring, IET Radar, Sonar & Navigation, 8, 776–786, https://doi.org/10.1049/iet-rsn.2013.0053, 2014.

Brisbourne, A. M., Martín, C., Smith, A. M., Baird, A. F., Kendall, J. M., and Kingslake, J.: Constraining Recent Ice Flow History at Korff Ice Rise, West Antarctica, Using Radar and Seismic Measurements of Ice Fabric, Journal of Geophysical Research: Earth Surface, 124,
435 175–194, https://doi.org/10.1029/2018JF004776, 2019.

Calonne, N., Montagnat, M., Matzl, M., and Schneebeli, M.: The layered evolution of fabric and microstructure of snow at Point Barnola, Central East Antarctica, Earth and Planetary Science Letters, 460, 293–301, https://doi.org/10.1016/j.epsl.2016.11.041, 2017.

Conway, H. and Rasmussen, L. A.: Recent thinning and migration of the Western Divide, central West Antarctica, Geophysical Research Letters, 36, 1–5, https://doi.org/10.1029/2009GL038072, 2009.

440 Corr, H. F. J., Jenkins, A., Nicholls, K. W., and Doake, C. S. M.: Precise measurement of changes in ice-shelf thickness by phase-sensitive radar to determine basal melt rates, Geophysical Research Letters, 29, 1–4, https://doi.org/10.1029/2001GL014618, 2002.

Cuffey, K. and Paterson, W. S.: The Physics of Glaciers, Academic Press, Amsterdam, fourth edn., 2010.

Dall, J.: Ice sheet anisotropy measured with polarimetric ice sounding radar, in: 30th International Geoscience and Remote Sensing Symposium (IGARSS 2010), pp. 2507–2510, Honolulu, HI, https://doi.org/10.1109/IGARSS.2010.5653528, 2010.

445 Davis, P. E., Jenkins, A., Nicholls, K. W., Brennan, P. V., Abrahamsen, E. P., Heywood, K. J., Dutrieux, P., Cho, K. H., and Kim, T. W.: Variability in Basal Melting Beneath Pine Island Ice Shelf on Weekly to Monthly Timescales, Journal of Geophysical Research: Oceans, 123, 8655–8669, https://doi.org/10.1029/2018JC014464, 2018.

DiPrinzio, C. L., Wilen, L. A., Alley, R. B., Fitzpatrick, J. J., Spencer, M. K., and Gow, A. J.: Fabric and texture at Siple Dome, Antarctica, Journal of Glaciology, 51, 281–290, https://doi.org/10.3189/172756505781829359, 2005.

450 Doake, C. S., Corr, H. F., and Jenkins, A.: Polarization of radio waves transmitted through Antarctic ice shelves, Annals of Glaciology, 34, 165–170, https://doi.org/10.3189/172756402781817572, 2002.

Doake, C. S. M., Corr, H. F., Jenkins, A., Nicholls, K. W., and Stewart, C. L.: Interpretation of polarimetric ice penetrating radar data over Antarctic ice shelves, in: FRISP Report, vol. 14, pp. 1–14, 2003.

Drews, R., Eisen, O., Steinhage, D., Weikusat, I., Kipfstuhl, S., and Wilhelms, F.: Potential mechanisms for anisotropy in ice-penetrating
455 radar data, Journal of Glaciology, 58, https://doi.org/10.3189/2012JoG11J114, 2012.

Durand, G., Gillet-Chaulet, F., Svensson, A., Gagliardini, O., Kipfstuhl, S., Meyssonnier, J., Parrenin, F., Duval, P., and Dahl-Jensen, D.: Change in ice rheology during climate variations - Implications for ice flow modelling and dating of the EPICA Dome C core, Climate of the Past, 3, 155–167, https://doi.org/10.5194/cp-3-155-2007, 2007.

Eisen, O., Hamann, I., Kipfstuhl, S., Steinhage, D., and Wilhelms, F.: Direct evidence for continuous radar reflector originating from changes
460 in crystal-orientation fabric, Cryosphere, 1, 1–10, https://doi.org/10.5194/tc-1-1-2007, 2007.

Fegyveresi, J. M., Alley, R. B., Fitzpatrick, J. J., Cuffey, K. M., McConnell, J. R., Voigt, D. E., Spencer, M. K., and Stevens, N. T.: Five millennia of surface temperatures and ice core bubble characteristics from the WAIS Divide deep core, West Antarctica, Paleoceanography, 31, 416–433, https://doi.org/10.1002/2015PA002851, 2016.

Fitzpatrick, J. J., Voigt, D. E., Fegyveresi, J. M., Stevens, N. T., Spencer, M. K., Cole-Dai, J., Alley, R. B., Jardine, G. E., Cravens, E. D., Wilen, L. A., Fudge, T. J., and McConnell, J. R.: Physical properties of the WAIS divide ice core, Journal of Glaciology, 60, 1140–1154, https://doi.org/10.3189/2014JoG14J100, 2014.

Fudge, T. J., Steig, E. J., Markle, B. R., Schoenemann, S. W., Ding, Q., Taylor, K. C., McConnell, J. R., Brook, E. J., Sowers, T., White, J. W., Alley, R. B., Cheng, H., Clow, G. D., Cole-Dai, J., Conway, H., Cuffey, K. M., Edwards, J. S., Lawrence Edwards, R., Edwards, R., Fegyveresi, J. M., Ferris, D., Fitzpatrick, J. J., Johnson, J., Hargreaves, G., Lee, J. E., Maselli, O. J., Mason, W., McGwire, K. C., Mitchell, L. E., Mortensen, N., Neff, P., Orsi, A. J., Popp, T. J., Schauer, A. J., Severinghaus, J. P., Sigl, M., Spencer, M. K., Vaughn, B. H., Voigt, D. E., Waddington, E. D., Wang, X., and Wong, G. J.: Onset of deglacial warming in West Antarctica driven by local orbital forcing, Nature, 500, 440–444, https://doi.org/10.1038/nature12376, 2013.

Fujita, S., Matsuoka, T., Ishida, T., Matsuoka, K., and Mae, S.: A summary of the complex dielectric permittivity of ice in the megahertz range and its applications for radar sounding of polar ice sheets, in: Physics of Ice Core Records, edited by Hondoh, T., pp. 185–212, Hokkaido University Press, Sapporo, Japan, 2000.

Fujita, S., Maeno, H., and Matsuoka, K.: Radio-wave depolarization and scattering within ice sheets: A matrix-based model to link radar and ice-core measurements and its application, Journal of Glaciology, 52, 407–424, https://doi.org/10.3189/172756506781828548, 2006.

Fujita, S., Okuyama, J., Hori, A., and Hondoh, T.: Metamorphism of stratified firn at Dome Fuji, Antarctica: A mechanism for local insolation modulation of gas transport conditions during bubble close off, Journal of Geophysical Research: Earth Surface, 114, 1–21, https://doi.org/10.1029/2008JF001143, 2009.

Gillet-Chaulet, F., Hindmarsh, R. C. A., Corr, H. F. J., King, E. C., and Jenkins, A.: In-situ quantification of ice rheology and direct measurement of the Raymond Effect at Summit, Greenland using a phase-sensitive radar, Geophysical Research Letters, 38, https://doi.org/10.1029/2011GL049843, 2011.

Gregory, S. A., Albert, M. R., and Baker, I.: Impact of physical properties and accumulation rate on pore close-off in layered firn, Cryosphere, 8, 91–105, https://doi.org/10.5194/tc-8-91-2014, 2014.

Gusmeroli, A., Pettit, E. C., Kennedy, J. H., and Ritz, C.: The crystal fabric of ice from full-waveform borehole sonic logging, Journal of Geophysical Research: Earth Surface, 117, 1–13, https://doi.org/10.1029/2012JF002343, 2012.

Hargreaves, N. D.: The polarization of radio signals in the radio echo sounding of ice sheets, Journal of Physics D: Applied Physics, 10, 1285–1304, https://doi.org/10.1088/0022-3727/10/9/012, 1977.

Hargreaves, N. D.: The Radio-Frequency Birefringence of Polar Ice, Journal of Glaciology, 21, 301–313, https://doi.org/10.3189/s0022143000033499, 1978.

Haynes, M. S., Chapin, E., and Schroeder, D. M.: Geometric power fall-off in radar sounding, IEEE Transactions on Geoscience and Remote Sensing, 56, 6571–6585, https://doi.org/10.1109/TGRS.2018.2840511, 2018.

Horgan, H. J., Anandakrishnan, S., Alley, R. B., Burkett, P. G., and Peters, L. E.: Englacial seismic reflectivity: Imaging crystal-orientation fabric in West Antarctica, Journal of Glaciology, 57, 639–650, https://doi.org/10.3189/002214311797409686, 2011.

Howat, I. M., Porter, C., Smith, B. E., Noh, M.-J., and Morin, P.: The Reference Elevation Model of Antarctica, The Cryosphere, 13, 665–674, https://doi.org/10.5194/tc-2018-240, 2019.

IPCC: Climate Change 2013: The Physical Science Basis, Cambridge University Press, Cambridge, United Kingdom and New York, NY, USA, fifth edn., 2013.

500   Jenkins, A., Corr, H. F. J., Nicholls, K. W., Stewart, C. L., and Doake, C. S. M.: Interactions between ice and ocean observed with phase-sensitive radar near an Antarctic ice-shelf grounding line, Journal of Glaciology, 52, 325–346, https://doi.org/10.3189/172756506781828502, 2006.

Jordan, T. M., Schroeder, D. M., Castelletti, D., Li, J., and Dall, J.: A Polarimetric Coherence Method to Determine Ice Crystal Orientation Fabric From Radar Sounding: Application to the NEEM Ice Core Region, IEEE Transactions on Geoscience and Remote Sensing, pp. 1–17, https://doi.org/10.1109/tgrs.2019.2921980, 2019.

Jordan, T. M., Besson, D. Z., Kravchenko, I., Latif, U., Madison, B., Nokikov, A., and Shultz, A.: Modeling ice birefringence and oblique radio wave propagation for neutrino detection at the South Pole, Annals of Glaciology, pp. 1–8, https://doi.org/10.1017/aog.2020.18, 2020a.

Jordan, T. M., Schroeder, D. M., Elsworth, C. W., and Siegfried, M. R.: Estimation of ice fabric within Whillans Ice Stream using polarimetric
510   phase-sensitive radar sounding, Annals of Glaciology, https://doi.org/10.1017/aog.2020.6, 2020b.

Kendrick, A. K., Schroeder, D. M., Chu, W., Young, T. J., Christoffersen, P., Todd, J., Doyle, S. H., Box, J. E., Hubbard, A., Hubbard, B., Brennan, P. V., Nicholls, K. W., and Lok, L. B.: Surface Meltwater Impounded by Seasonal Englacial Storage in West Greenland, Geophysical Research Letters, pp. 474–481, https://doi.org/10.1029/2018GL079787, 2018.

Kennedy, J. H., Pettit, E. C., and Di Prinzio, C. L.: The evolution of crystal fabric in ice sheets and its link to climate history, Journal of
515   Glaciology, 59, 357–373, https://doi.org/10.3189/2013JoG12J159, 2013.

Kingslake, J., Hindmarsh, R. C. A., Aalgeirsdõttir, G., Conway, H., Corr, H. F. J., Gillet-Chaulet, F., Martín, C., King, E. C., Mulvaney, R., and Pritchard, H. D.: Full-depth englacial vertical ice sheet velocities measured using phase-sensitive radar, Journal of Geophysical Research F: Earth Surface, 119, 2604–2618, https://doi.org/10.1002/2014JF003275, 2014.

Kingslake, J., Martín, C., Arthern, R. J., Corr, H. F., and King, E. C.: Ice-flow reorganization in West Antarctica 2.5 kyr ago dated using
520   radar-derived englacial flow velocities, Geophysical Research Letters, 43, 9103–9112, https://doi.org/10.1002/2016GL070278, 2016.

Kluskiewicz, D., Waddington, E. D., Anandakrishnan, S., Voigt, D. E., Matsuoka, K., and McCarthy, M. P.: Sonic methods for measuring crystal orientation fabric in ice, and results from the West Antarctic ice sheet (WAIS) Divide, Journal of Glaciology, 63, 603–617, https://doi.org/10.1017/jog.2017.20, 2017.

Koutnik, M. R., Fudge, T. J., Conway, H., Waddington, E. D., Neumann, T. A., Cuffey, K. M., Buizert, C., and Taylor, K. C.: Holocene
525   accumulation and ice flow near the West Antarctic Ice Sheet Divide ice core site, Journal of Geophysical Research: Earth Surface, 121, 907–924, https://doi.org/10.1002/ 2015JF003668, 2016.

Li, J., González, J. A., Leuschen, C., Harish, A., Gogineni, P., Montagnat, M., Weikusat, I., Rodriguez-Morales, F., and Paden, J.: Multichannel and multi-polarization radar measurements around the NEEM site, Cryosphere, 12, 2689–2705, https://doi.org/10.5194/tc-12-2689-2018, 2018.

530   Lindbäck, K., Moholdt, G., Nicholls, K. W., Hattermann, T., Pratap, B., Thamban, M., and Matsuoka, K.: Spatial and temporal variations in basal melting at Nivlisen ice shelf, East Antarctica, derived from phase-sensitive radars, The Cryosphere, 13, 2579–2595, https://doi.org/10.5194/tc-13-2579-2019, 2019.

Marsh, O. J., Fricker, H. A., Siegfried, M. R., and Christianson, K.: High basal melt rates initiate a channel at the grounding line of Ross Ice Shelf, Antarctica, Geophysical Research Letters, 43, 250–255, https://doi.org/10.1002/2015GL066612.Received, 2016.

535   Matsuoka, K., Furukawa, T., Fujita, S., Maeno, H., Uratsuka, S., Naruse, R., and Watanabe, O.: Crystal orientation fabrics within the
Antarctic ice sheet revealed by a multipolarization plane and dual-frequency radar survey, Journal of Geophysical Research, 108, 10,
https://doi.org/10.1029/2003JB002425, 2003.

Matsuoka, K., Wilen, L., Hurley, S. P., and Raymond, C. F.: Effects of birefringence within ice sheets on obliquely propagating radio waves,
IEEE Transactions on Geoscience and Remote Sensing, 47, 1429–1443, https://doi.org/10.1109/TGRS.2008.2005201, 2009.

540   Matsuoka, K., Power, D., Fujita, S., and Raymond, C. F.: Rapid development of anisotropic ice-crystal-alignment fabrics in-
ferred from englacial radar polarimetry, central West Antarctica, Journal of Geophysical Research: Earth Surface, 117, 1–16,
https://doi.org/10.1029/2012JF002440, 2012.

Montagnat, M., Azuma, N., Dahl-Jensen, D., Eichler, J., Fujita, S., Gillet-Chaulet, F., Kipfstuhl, S., Samyn, D., Svensson, A., and Weikusat,
I.: Fabric along the NEEM ice core, Greenland, and its comparison with GRIP and NGRIP ice cores, Cryosphere, 8, 1129–1138,
545   https://doi.org/10.5194/tc-8-1129-2014, 2014.

Morlighem, M., Rignot, E., Binder, T., Blankenship, D., Drews, R., Eagles, G., Eisen, O., Ferraccioli, F., Forsberg, R., Fretwell, P., Goel,
V., Greenbaum, J. S., Gudmundsson, H., Guo, J., Helm, V., Hofstede, C., Howat, I., Humbert, A., Jokat, W., Karlsson, N. B., Lee, W. S.,
Matsuoka, K., Millan, R., Mouginot, J., Paden, J., Pattyn, F., Roberts, J., Rosier, S., Ruppel, A., Seroussi, H., Smith, E. C., Steinhage,
D., Sun, B., van den Broeke, M. R., van Ommen, T. D., van Wessem, M., and Young, D. A.: Deep glacial troughs and stabilizing ridges
550   unveiled beneath the margins of the Antarctic ice sheet, Nature Geoscience, 13, 132–137, https://doi.org/10.1038/s41561-019-0510-8,
2020.

Mott, H.: Remote Sensing with Polarimetric Radar, John Wiley & Sons Inc, New York, NY, USA, https://doi.org/10.1002/0470079819, 2006.

Nicholls, K. W., Corr, H. F. J., Stewart, C. L., Lok, L. B., Brennan, P. V., and Vaughan, D. G.: Instruments and methods: A ground-based
radar for measuring vertical strain rates and time-varying basal melt rates in ice sheets and shelves, Journal of Glaciology, 61, 1079–1087,
555   https://doi.org/10.3189/2015JoG15J073, 2015.

Nicolas, J. P. and Bromwich, D. H.: Climate of West Antarctica and Influence of Marine Air Intrusions, Journal of Climate, 24, 49–67,
https://doi.org/10.1175/2010JCLI3522.1, 2011.

Paterson, W. S.: Why ice-age ice is sometimes "soft", Cold Regions Science and Technology, 20, 75–98, https://doi.org/10.1016/0165-
232X(91)90058-O, 1991.

560   Scott, R. C., Nicolas, J. P., Bromwich, D. H., Norris, J. R., and Lubin, D.: Meteorological Drivers and Large-Scale Climate Forcing of West
Antarctic Surface Melt, Journal of Climate, 32, 665–684, https://doi.org/10.1175/JCLI-D-18-0233.1, 2019.

Sigl, M., Fudge, T. J., Winstrup, M., Cole-Dai, J., Ferris, D., McConnell, J. R., Taylor, K. C., Welten, K. C., Woodruff, T. E., Adolphi,
F., Bisiaux, M., Brook, E. J., Buizert, C., Caffee, M. W., Dunbar, N. W., Edwards, R., Geng, L., Iverson, N., Koffman, B., Layman, L.,
Maselli, O. J., McGwire, K., Muscheler, R., Nishiizumi, K., Pasteris, D. R., Rhodes, R. H., and Sowers, T. A.: The WAIS Divide deep ice
565   core WD2014 chronology - Part 2: Annual-layer counting (0-31 ka BP), Climate of the Past, 12, 769–786, https://doi.org/10.5194/cp-12-
769-2016, 2016.

Stewart, C. L., Christoffersen, P., Nicholls, K. W., Williams, M. J., and Dowdeswell, J. A.: Basal melting of Ross Ice Shelf from solar heat
absorption in an ice-front polynya, Nature Geoscience, 12, 435–440, https://doi.org/10.1038/s41561-019-0356-0, 2019.

Sun, S., Hattermann, T., Pattyn, F., Nicholls, K. W., Drews, R., and Berger, S.: Topographic Shelf Waves Control Seasonal Melting Near
570   Antarctic Ice Shelf Grounding Lines, Geophysical Research Letters, 46, 9824–9832, https://doi.org/10.1029/2019GL083881, 2019.

Vaňková, I., Voytenko, D., Nicholls, K. W., Xie, S., Parizek, B. R., and Holland, D. M.: Vertical Structure of Diurnal Englacial Hydrology
Cycle at Helheim Glacier, East Greenland, Geophysical Research Letters, 45, 8352–8362, https://doi.org/10.1029/2018GL077869, 2018.

Vaňková, I., Nicholls, K. W., Corr, H. F. J., Makinson, K., and Brennan, P. V.: Observations of Tidal Melt and Vertical Strain at the Filchner-Ronne Ice Shelf, Antarctica, Journal of Geophysical Research: Earth Surface, 125, https://doi.org/10.1029/2019jf005280, 2020.

575 Wang, B., Sun, B., Martin, C., Ferraccioli, F., Steinhage, D., Cui, X., and Siegert, M. J.: Summit of the East Antarctic ice sheet underlain by thick ice-crystal fabric layers linked to glacial-interglacial environmental change, Geological Society, London, Special Publications, 461, 131–143, https://doi.org/10.1144/SP461.1, 2018.

Washam, P., Nicholls, K. W., Münchow, A., and Padman, L.: Summer surface melt thins Petermann Gletscher Ice Shelf by enhancing channelized basal melt, Journal of Glaciology, 65, 662–674, https://doi.org/10.1017/jog.2019.43, 2019.

580 Wilen, L. A., Diprinzio, C. L., Alley, R. B., and Azuma, N.: Development, principles, and applications of automated ice fabric analyzers, Microscopy Research and Technique, 62, 2–18, https://doi.org/10.1002/jemt.10380, 2003.

Young, T. J., Schroeder, D. M., Christoffersen, P., Lok, L. B., Nicholls, K. W., Brennan, P. V., Doyle, S. H., Hubbard, B., and Hubbard, A.: Resolving the internal and basal geometry of ice masses using imaging phase-sensitive radar, Journal of Glaciology, 64, 649–660, https://doi.org/10.1017/jog.2018.54, 2018.

585 Young, T. J., Christoffersen, P., Doyle, S. H., Nicholls, K. W., Stewart, C. L., Hubbard, B., Hubbard, A., Lok, L. B., Brennan, P. V., Benn, D. I., Luckman, A., and Bougamont, M.: Physical Conditions of Fast Glacier Flow: 3. Seasonally-Evolving Ice Deformation on Store Glacier, West Greenland, Journal of Geophysical Research: Earth Surface, 124, 245–267, https://doi.org/10.1029/2018JF004821, 2019.